scientific reports

Check for updates

OPEN

Spectral scattering characteristics of subwavelength-sized spherical particles near Mie resonance modes probed by tightly focused Terahertz waves

Da-Hye Choi

The complex dynamics of terahertz (THz) wave scattering by subwavelength-scale structures remain largely unexplored. This article examines the spectral scattering characteristics of subwavelength-sized spherical particles probed by tightly focused THz waves through numerical simulations and experimental techniques. The simulations reveal that the scattering intensity for lower Mie resonance modes (magnetic dipole and electric dipole modes) remains largely unaffected when THz waves are focused down to 0.3 λ, whereas higher Mie resonance modes experience a significant decrease in intensity as the beam size is reduced. Experimentally, scattering effects were observed by imaging two subwavelength-sized dielectric spheres, each with a diameter of 480 μm and refractive indices of 2 and 6, around 0.3 THz, where the magnetic dipole mode of the particle with refractive index of 2 was detected. Experimental results confirm that the image contrast of the spheres is predominantly influenced by scattering effects near the Mie resonance frequency, even with low refractive index materials. This work represents a significant advancement in the detection and characterization of subwavelength-sized structures within the THz region. Furthermore, the findings extend beyond THz frequency ranges and have potential applications in fields such as sensing, imaging, and sizing across optical, infrared, and millimeter wave ranges.

Electromagnetic wave scattering by subwavelength-sized particles has been a significant topic of scientific inquiry across the electromagnetic spectrum since Lord Rayleigh first explained why the sky is blue in 1871[1,2]. Later, Gustav Mie elucidated the color variations in colloidal solutions of gold nanoparticles based on their size distribution when the particle size is comparable to the wavelength[1]. Building upon this seminal work, Mie scattering continues to be extensively investigated for numerous applications, including dielectric resonators for nanophotonics[3,4], bioimaging with visible light[5], biological diagnostics utilizing Fourier transform infrared spectroscopy[6], and meteorology using millimeter waves[7].

Terahertz (THz) waves, which occupy the region between microwave and infrared waves in the electromagnetic spectrum, have also been widely studied for spectroscopy and imaging across various fields, including material science, non-destructive testing, and biomedical applications[8–10]. Effective medium theory (EMT) is frequently employed to characterize composite materials, such as powders, liquids, and biological tissues in the THz frequency range. The fundamental concept of EMT is that the macroscopic optical properties of a material can be derived from the optical properties and volume fractions of its individual constituents[11]. In this context, Mie scattering is typically neglected when characterizing composite materials. However, for EMT to provide accurate results, certain conditions must be met: the constituent materials must be subwavelength in size and homogeneously distributed[12,13]. These conditions are often not satisfied, requiring careful interpretation and application of EMT.

When the size of the constituents is comparable to the THz wavelength, Mie scattering becomes significant. Studies have shown that such scattering can induce resonant propagation loss in powder materials, such as mixtures of high-density polyethylene (HDPE) and fructose powders with grain sizes approximately equal to the THz wavelength[14]. Another study demonstrated that scattering can produce spurious resonances in the THz signatures of polytetrafluoroethylene (PTFE)-glass microspheres and PTFE-lactose composites[15]. In materials

Terahertz Research Section, Electronics and Telecommunications Research Institute, Deajeon 34129, Republic of Korea. email: choi.dh@etri.re.kr

with distinctive resonant features in the THz spectrum, such as explosives, narcotics, and sugar, scattering can obscure these inherent features[16]. Consequently, these materials are often ground into fine particles and pressed into pellets for investigation, which limits their practical applications[17].

Biological entities and tissues also contain structural elements, such as fat cells, tissue spheroids, and microfibrils, with dimensions similar to THz wavelengths[18–20]. Mie scattering effects from these elements can lead to misinterpretations of THz signals reflected or absorbed by biological tissues, thereby reducing the effectiveness of THz-based medical diagnostics[9]. Historically, Mie scattering in tissues at THz frequencies was assumed to be much weaker, with EMT traditionally used to describe THz-tissue interactions[21]. A recent study demonstrated both theoretically and experimentally that the optical properties of a tissue-mimicking phantom could be described by EMT under specific conditions: when scatterer diameters are smaller than 0.47 times the wavelength and volume fractions are smaller than 0.2[22].

However, compelling evidence supports the Mie-like nature of THz wave scattering in tissues. Polarization-sensitive THz imaging has proven valuable in distinguishing healthy and pathologically altered tissues, providing insights beyond the explanatory scope of EMT[23]. Despite extensive research on THz wave-tissue interactions, the intricate dynamics of THz wave scattering by wavelength-scale constituents in tissues, and the interplay between absorption and scattering phenomena, remain largely unexplored. A key challenge lies in the fact that direct observation of Mie scattering effects is challenging due to the small ratio of back-scattered THz waves relative to the incident waves and the narrow angular spread of the scattered waves[24]. Moreover, Mie scattering at the subwavelength scale has not been thoroughly investigated, mainly due to limitations in experimental methods. THz near-field imaging of Mie scattering has been studied in a transmission configuration for high-permittivity TiO_2 microspheres[25]. However, investigating biological systems, which often contain significant amounts of water, requires an experimental configuration in reflection mode capable of probing lower refractive index materials. Addressing these complexities - including the challenges of observing Mie scattering effects, the unexplored scattering dynamics in tissues, and the limitations of current experimental methods - is crucial for advancing our understanding of THz interactions in biological media and for optimizing their application in biomedical imaging and diagnostics.

Recently, we demonstrated a broadband subwavelength THz imaging system by combining a solid-immersion lens (SIL) with a THz time-domain spectrometer (TDS)[26,27]. As the SIL serves as an image resolution enhancer component, this system offers subwavelength imaging resolution across a wide spectral range (from 0.3 to 2.0 THz). In this paper, we investigated the spectral scattering characteristics of subwavelength-sized spherical particles with this imaging system and numerical simulations. Experimental results demonstrate that the near-field spectral images of the spheres are predominantly influenced by scattering effects near the Mie resonance frequency, even when utilizing low-refractive-index materials ($n=2$). This work represents a significant advancement in the detection and characterization of subwavelength-sized structures in the THz region. Moreover, the findings extend beyond THz frequency ranges and have potential applications in fields such as sensing, imaging, and sizing across the optical, infrared, and millimeter wave ranges.

Results and discussion

Simulated scattering characteristics of a subwavelength-sized sphere illuminated by plane wave

First, the scattering characteristics of a spherical particle with a diameter of 500 μm and a refractive index of 3.4, illuminated by a plane wave, were simulated using COMSOL Multiphysics (Fig. 1). This combination of diameter and refractive index was chosen as a representative case to validate the simulation by comparing the results with analytical calculations and to demonstrate the electric field distribution of the resonance modes. An exact analytical solution to Maxwell's equations exists for this scenario[1]. The scattering cross section is given by:

$$\sigma_{sc} = \frac{\lambda^2}{2\pi}\sum_{m=1}^{\infty}(2m+1)\left(|a_m|^2+|b_m|^2\right), \tag{1}$$

where λ represents the wavelength, and a_m and b_m denote the electric and magnetic multipoles of order m, respectively. The simulated scattering cross section of the spherical particle is shown in Fig. 1b, demonstrating consistency with the analytical solution. The first peak at 168 GHz corresponds to the magnetic dipole (MD) resonance, which arises from the coupling of the incident THz wave to the circular displacement currents in the electric field. This resonance occurs when the wavelength inside the particle is comparable to the particle's diameter ($d \approx \lambda/n$), consistent with previous literature[3,28,29]. The electric field profiles of the three peaks in the scattering cross section at lower frequencies, shown in Fig. 1c–e, confirm that these peaks correspond to the MD, electric dipole (ED), and electric quadrupole (EQ) Mie resonance modes[28,30]. The characteristics of higher-order modes are beyond the scope of this study.

Simulated scattering characteristics of subwavelength-sized spheres illuminated by Gaussian beams

As outlined in the introduction, the experimental observation of Mie scattering effects in typical THz imaging systems is challenging due to the low energy and narrow angular distribution of back-scattered THz waves. Additionally, subwavelength-scale structures often remain unresolved, leading to undetected Mie scattering effects in THz imaging[26]. To experimentally assess the impact of Mie scattering on THz imaging of subwavelength-scale structures, we employed our recently developed broadband subwavelength THz imaging system[26,27]. Since this system utilizes tightly focused THz waves, we conducted numerical simulations to explore how the scattering spectra and internal electric field distribution of spherical particles are affected when the

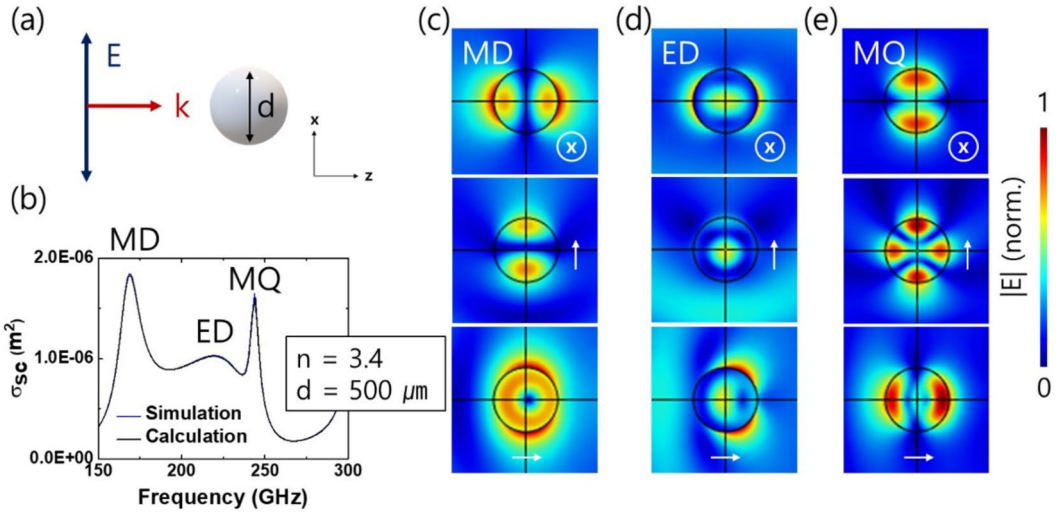

Fig. 1. (**a**) Incident field vector and a subwavelength-sized spherical particle used in the simulations. (**b**) Calculated and simulated scattering cross section, σ_{sc}, of a particle with a diameter d = 2a = 500 μm and refractive index $n = 3.4$. Spatial distribution of the scattered electric field amplitude for the (**c**) magnetic dipole (MD), (**d**) electric dipole (ED), and (**e**) magnetic quadrupole (MQ) modes. The direction of the wave propagation is indicated in the electric field profiles.

incident wave shifts from a plane wave to a Gaussian beam. The Gaussian beam was modeled with diameters of 3.3, 1.0, and 0.3 λ, across refractive indices $n = 2$, 3.4, and 6 for a sphere with a fixed diameter at 500 μm.

Figure 2 shows the scattering cross sections under different illumination conditions and refractive indices. In general, the scattering cross section increases with the refractive index n, consistent with the literature[3,28,29]. For a beam diameter of 3.3 λ, the scattering cross sections and electric field profiles closely match those of the plane wave scenario for all simulated refractive indices. As the beam diameter decreases, the scattering cross sections decrease correspondingly. For $n = 3.4$ and 6, the first and second modes (MD and ED) remain largely unaffected by the reduction in beam size, while the MQ mode intensity diminishes significantly as the beam diameter approaches the wavelength. The electric field profiles confirm that the MD and ED modes are maintained, while the MQ mode field concentrates towards the sphere's center under reduced beam size conditions (the electric field profiles for the ED modes are not shown for simplicity). We conclude that dipole modes are preserved in both scattering intensity and electric field profiles when the beam size is reduced within our simulation conditions.

Experimental validation

Experimentally, near-field spectral images of a subwavelength-sized spherical particle are obtained by performing a 2D scan, focusing the Gaussian beam on different areas of the particle. To better understand the experimental results, simulations of scattering characteristics at various illumination positions were conducted. Figure 3 presents the scattering behavior of a dielectric sphere with a diameter of 500 μm and refractive indices of 2 and 6, using a Gaussian beam with a fixed diameter of 0.3 λ. Figure 3a–c show that, for a sphere with a refractive index of 2, the frequency-dependent scattering decreases in overall magnitude, accompanied by a slight shift in the peak frequency to a lower frequency region under off-center and edge illumination. In contrast, Fig. 3g–i present the results for a sphere with a refractive index of 6, where the scattering intensity decreases under off-center and edge illumination without significant changes in the peak frequency.

We also simulated the electric field directly in front of the illuminated region of the sphere, aligning with the center of the illuminating Gaussian beam, as shown in Fig. 3d–f, j–l to facilitate comparison with the experimental results. Domain point probes were used to monitor the scattered electric field. Across all illumination conditions, the amplitude of the scattered electric field exhibited fluctuations near the Mie resonance mode. Notably, the most significant fluctuations occurred under center illumination for both refractive index values, while edge illumination resulted in a relatively flat field spectrum. These findings suggest that, in near-field spectral imaging, the central region of the particle is optimal for detecting Mie scattering effects. Additionally, at specific frequencies, the edge of the particle may appear brighter than the center. Such image distortions, unrelated to the inherent optical properties of the sphere, must be carefully considered when imaging subwavelength-sized microstructures.

The scattering effects were experimentally visualized by probing two spherical particles, each with a diameter of 480 μm and refractive indices of 2 and 6 around 0.3 THz. At this frequency, the MD mode of the $n = 2$ particle is present. The experimental setup used is described above. One particle was a glass bead (Sigma-Aldrich, USA), and the other was a zirconia ball (Labkom, Republic of Korea). The particles were affixed to adhesion tape, mounted free-standing on optical supports, as shown in Fig. 4a, and loaded onto two-dimensional translation stages for a 2D scan. During the scan, THz time domain (TD) signals were recorded at each position. The TD signals reflected from the center of the particles are shown in Fig. 4b. The signals prior to 0 ps have been

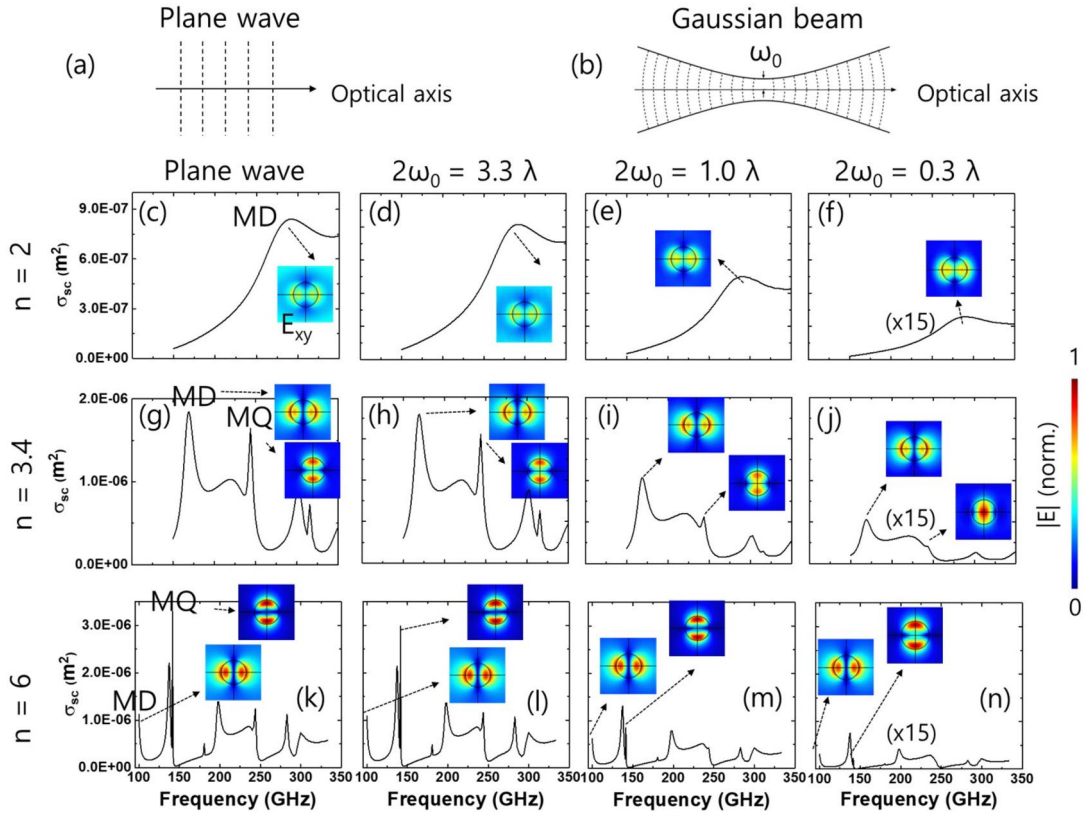

Fig. 2. Schematic of the (**a**) plane wave and (**b**) focused (Gaussian) beam. (**c–n**) Beam size-dependent scattering cross section σ_{sc} of a dielectric sphere with a diameter of 500 μm and refractive indices 2, 3.4, and 6 (from top to bottom). The electric field profile in the xy-plane (E_{xy}) at several Mie resonance modes is shown.

truncated; otherwise, the much larger reflection from the planar surface of the SIL would dominate, obscuring the spectral characteristics of the particles[26,27]. At approximately 1 ps, a sharp peak was observed for both particles, corresponding to reflections at the air-particle interfaces. At around 8 and 20 ps, peaks were detected for particles 1 ($n=2$) and 2 ($n=6$), respectively, corresponding to reflections at the particle-tape interfaces. Spectral images were generated by applying fast Fourier transform (FFT) to the TD signals[26,27].

Figure 4c,e,g illustrate the spectral images of the particles as the measurement time span varied. When the time window was limited to 4 ps, the center of particle 2, which has a higher refractive index, appeared brighter across all investigated frequencies. The amplitude at the particle center, as a function of frequency, is shown in Fig. 4d. With the time window extended to 12 ps, a resonance (magnetic dipole mode) became visible in the field spectrum for particle 1 around 280 GHz, with the field concentrated within the particle, making the center of particle 1 brighter than that of particle 2. With a further extension of the time window to 22 ps, more complex results were observed. The spectral field amplitude of particle 1 became oscillatory due to the multiple reflections inside the particle (Fig. 4h). At f_1 (240 GHz), particle 2 was brighter than particle 1, while at f_2 (280 GHz) and f_3 (320 GHz), particle 1 was brighter than particle 2. Note that the particles exhibited minimal dispersion within the investigated frequency ranges[31,32], indicating that the frequency-specific image contrast arises primarily from the geometrical properties of the particles. Additionally, frequency-specific scattering effects are highly dependent on the measurement time window, indicating that both the frequency range and the measurement time window can be optimized to improve image contrast and reduce artificial effects.

We further simulated the scattered field spectrum of the particles under experimental conditions to compare with the experiment results. Incident THz waves were modeled as Gaussian beams, as they provide a good approximation of THz waves in TDS systems[33–35]. The beam size, $2\omega_0$, was set to 0.3 λ, as measured in our previous study[26]. The THz waves were obliquely incident on the particles, which were attached to adhesion tape. The refractive indices of the particles were 2 and 6, respectively, and loss was neglected according to literature values[31,32]. The refractive index of the tape was measured as 1.55, using a previously reported measurement and analysis method[36], and applied in the simulation. Figure 5 compares the measured field amplitude with the simulated field amplitude at the center of the particles. Since the simulation does not account for effects from multiple reflections inside the particle, the measurement time windows were set to 12 ps for particle 1 and 22 ps for particle 2, respectively. The field spectrum of particle 1 ($n=2$) exhibits a broad peak around 280 GHz, corresponding to the MD mode, as shown in Fig. 5. For particle 2, a peak around 240 GHz and valleys around 270 and 320 GHz are reproduced, though the simulation shows a slight shift toward higher frequency regions. This shift can be attributed to variations in the image plane position, discrepancies in beam size between the experiment and simulation, inaccuracies in the angle of incidence used in both, and measurement uncertainties in

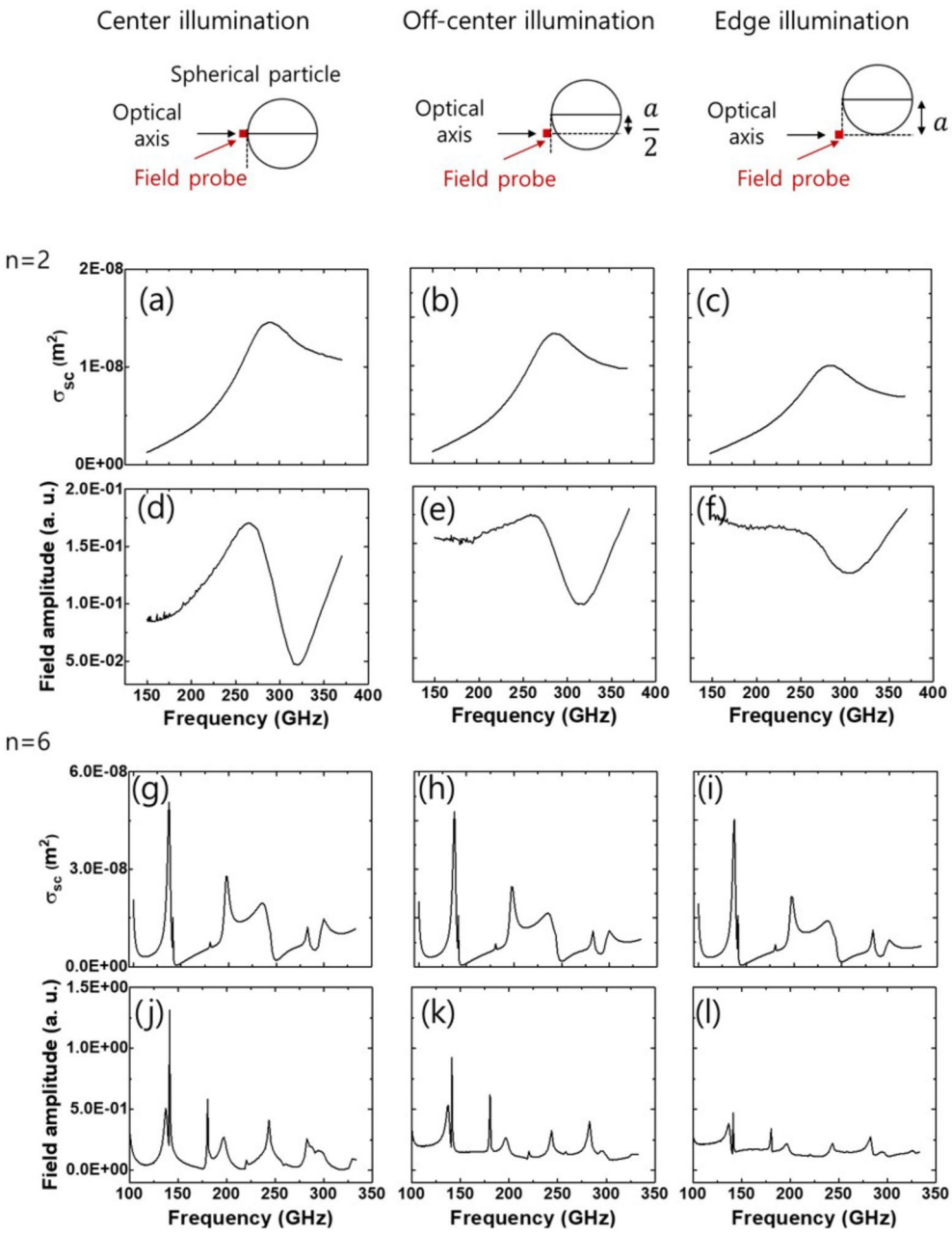

Fig. 3. (**a–c**) Scattering cross section (σ_{sc}) of a spherical particle with a diameter of 500 μm and a refractive index of 2 under different illumination positions: center, off-center, and edge illumination (left to right). (**d–f**) Field amplitude measured in front of the particle for the same illumination positions. (**g–i**) Scattering cross section of a spherical particle with a diameter of 500 μm and a refractive index of 6 under identical illumination positions. (**j–l**) Field amplitude measured in front of the particle for each illumination position.

the size and optical constants of the particles. Additionally, for particle 2 ($n = 6$), complex higher-order modes are observed within the analyzed range, complicating the comparison between experimental and simulation results. For instance, simulations around 300 GHz reveal peaks resulting from strong field confinement associated with the higher-order mode, whereas the experimental data do not effectively capture these characteristics. Although a detailed examination of these higher-order modes lies beyond the scope of this study, their investigation offers a promising direction for future research and is expected to provide valuable insights into the field dynamics.

Conclusion

In conclusion, we investigated the spectral scattering characteristics of subwavelength-sized spherical particles imaged by tightly focused THz waves using both numerical simulations and experimental methods. The numerical simulations indicated that the intensity of the scattering spectrum for lower Mie resonance modes (MD and ED modes) remains largely unchanged when incident THz waves are focused down to 0.3 λ, whereas

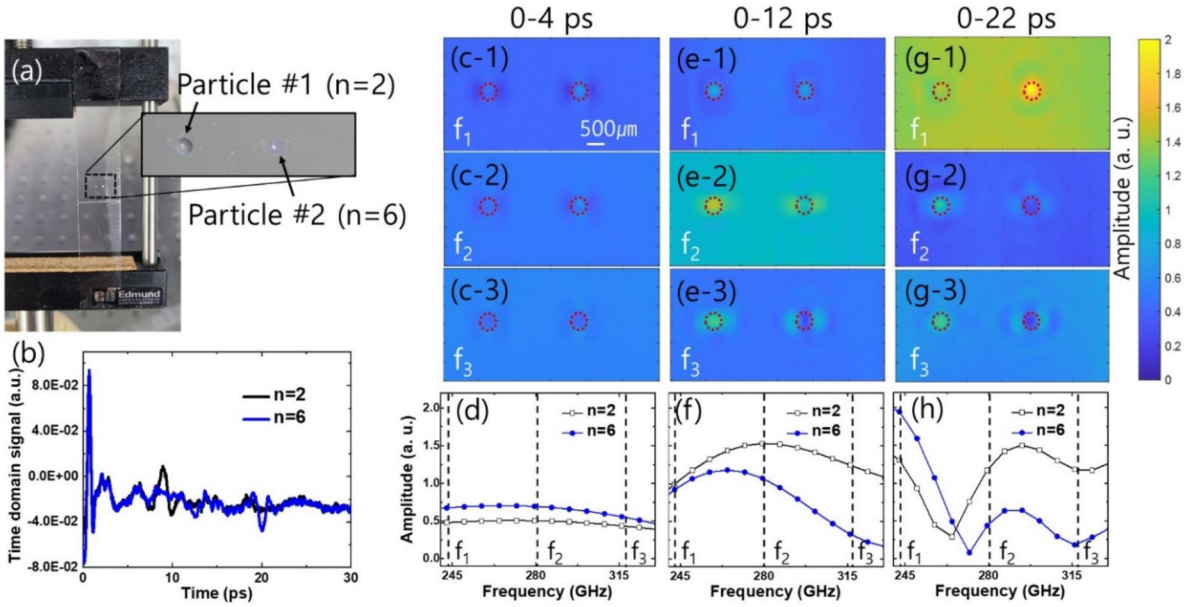

Fig. 4. (**a**) Photograph of spherical particles supported by adhesion tape. (**b**) Measured time-domain signals reflected at the center of the particles. (**c**,**e**,**g**) Near-field imaging of the spheres in the frequency-domain, each with a diameter of 480 μm and refractive indices of 2 (left) and 6 (right), under different measurement conditions. Dotted red circles indicate particle positions. The images are presented at three frequencies: f_1 (240 GHz), f_2 (280 GHz), and f_3 (320 GHz), across three different time spans: 0–4 ps, 0–12 ps, and 0–22 ps (from left to right). (d, f, and h) Measured electric near-field spectra in front of the particles at different measurement time windows.

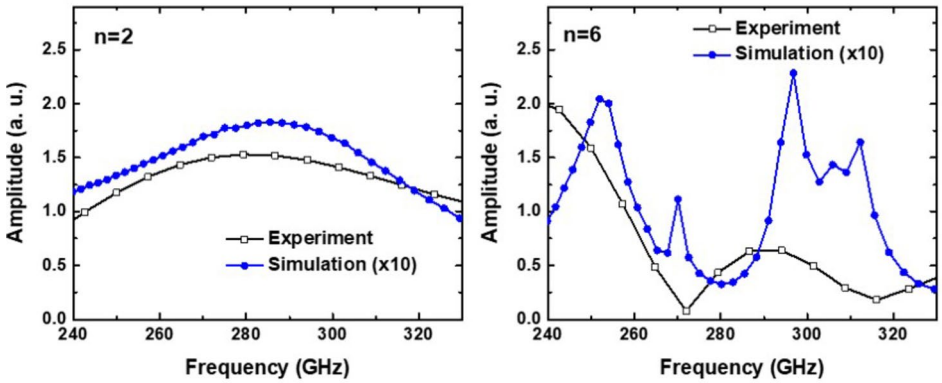

Fig. 5. Comparison between the measured and simulated spectra at the center of the spherical particles with refractive indices of 2 (left) and 6 (right), both with a diameter of 480 μm.

higher Mie resonance modes exhibit a significant decrease in intensity as the beam size is reduced. The simulation specifically examined spherical particles with a diameter of 500 μm and refractive indices of 2, 3.4, and 6 in the THz region.

The scattering effects were experimentally visualized by probing two dielectric spheres with a diameter of 480 μm and refractive indices of 2 and 6 around 300 GHz. One of the key findings of this study is the observation of a resonance, identified as the MD mode in the simulation, becoming visible in the measured field spectrum for particle 1 ($n=2$) at approximately 280 GHz. In this mode, the field is concentrated within the particle, causing the center of particle 1—characterized by a lower refractive index and lower reflection coefficient—to appear brighter than that of particle 2 ($n=6$). Furthermore, the simulation results provide reasonable predictions of the experimental outcomes regarding the peaks and valleys in the field spectrum.

We also demonstrate that frequency-specific scattering effects are highly dependent on the measurement time window, suggesting that both the frequency range and the measurement time window can be optimized to enhance image contrast and minimize artificial effects. This work represents a significant advancement in the detection and characterization of subwavelength-sized heterostructures in the THz region. Based on these

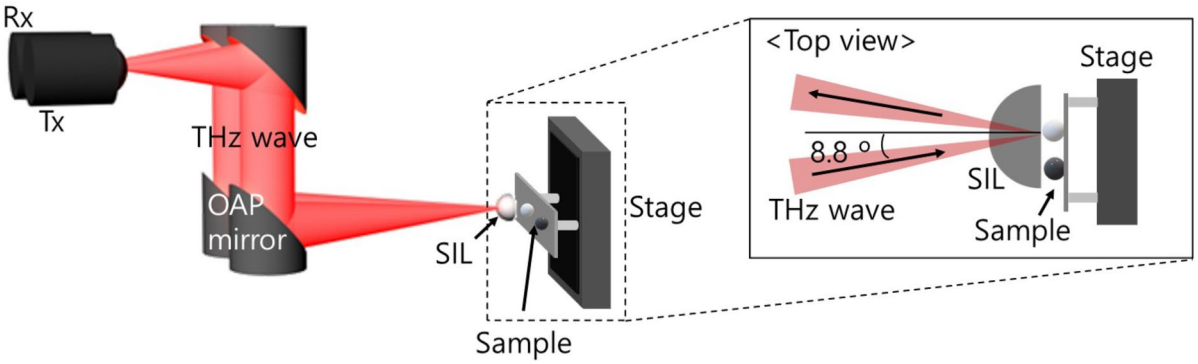

Fig. 6. Schematic of the experimental setup. The emitter (Tx) and detector (Rx) are fiber-coupled photoconductive antennas for the generation and detection of THz waves, respectively. Off-Axis Parabolic (OAP) mirrors are used to collimate and focus the THz waves. The focused THz waves are obliquely incident at an angle of 8.8° to the objects and are reflected into the Rx. The object is mounted on two motorized stages for a two-dimensional raster scan.

findings, further investigation into biological systems could provide valuable insights into subwavelength tissue heterogeneities, facilitate the diagnosis of malignant and benign neoplasms, and enable more accurate delineation of tumor margins. Moreover, the findings extend beyond THz frequency ranges and can be applied in various fields, such as sensing, imaging, and sizing across optical, infrared, and millimeter wave ranges.

Methods

Experimental set up

Figure 6 illustrates a schematic of the experimental setup. In the experiment, we employed a commercial THz TDS (TERA K15, Menlo Systems, Germany) integrated with a SIL in a reflection configuration, as previously reported[26,27]. THz waves generated by the emitter (Tx) were collimated and focused by off-axis parabolic (OAP) mirrors before being directed toward the object at an angle of 8.8°. The reflected THz waves were subsequently collimated and focused by identical OAP mirrors, and then detected by the detector (Rx). A hemispherical high-resistivity float-zone (HRFZ) silicon lens with a radius of 5 mm served as the SIL, reducing the THz beam size across a broad spectral range.

Subwavelength-sized spherical particles, attached to adhesion tape, were placed on a two-axis motorized stage (M-403.6PD, PI, Germany), enabling a 2D raster scan to investigate spectral scattering characteristics of subwavelength-scale particles. The SIL-to-object distance was approximately 10 μm throughout the experiments. At each measurement position, a TD signal reflected from the object was acquired. Object information in the frequency domain was obtained by applying FFT to the measured THz TD signal[26,27]. This process is repeated during a 2D scan of the object to construct a near-field 2D image of the object across various frequencies, typically within the frequency range of 0.2–2 THz. The experiments were conducted in dry air conditions to enhance the signal-to-noise ratio of the acquired images.

Simulation

This study employed COMSOL Multiphysics to simulate the spectral scattering characteristics of subwavelength-sized spherical particles illuminated by THz waves. The incident wave was polarized in the x-direction and propagated in the z-direction. Scattered THz waves were calculated for various particles and illumination conditions. A Perfectly Matched Layer (PML) boundary condition was applied to the outer boundaries of the simulation domain to prevent unphysical scattering from the boundaries. The wavelengths of the THz waves were varied to obtain the spectral scattering characteristics of the particles.

Data availability

The dataset generated during and/or analyzed during the current study are available from the corresponding author on reasonable request.

Received: 15 October 2024; Accepted: 1 January 2025
Published online: 07 January 2025

References

1. Bohren, C. F. & Huffman, D. R. *Absorption and Scattering of Light by Small Particles* (Wiley, 1983).
2. Krasnok, A. et al. Anomalies in light scattering. *Adv. Opt. Photon.* **11** (4), 892–951 (2019).
3. Kuznetsov, A. I., Miroshnichenko, A. E., Brongersma, M. L. & Kivshar, Y. S. Luk'yanchuk, B. optically resonant dielectric nanostructures. *Science* **354** (6314), aag2472 (2016).
4. Koshelev, K. et al. Subwavelength dielectric resonators for nonlinear nanophotonics. *Science* **367** (6475), 288–292 (2020).
5. Adachi, M. et al. Fluorophore-decorated mie resonant silicon nanosphere for scattering/fluorescence dual-mode imaging. *Small* **19** (14), 2207318 (2023).
6. Baker, M. J. et al. Using Fourier transform IR spectroscopy to analyze biological materials. *Nat. Protoc.* **9** (8), 1771–1791 (2014).

7. Kollias, P., Albrecht, B. A. & Marks, F. Jr Why Mie? Accurate observations of vertical air velocities and raindrops using a cloud radar. *Bull. Am. Meteorol. Soc.* **83** (10), 1471–1484 (2002).
8. Mittleman, D. M. Twenty years of terahertz imaging. *Opt. Express* **26** (8), 9417–9431 (2018).
9. Marklez, A. G. & Mittleman, D. M. Perspective on terahertz applications in bioscience and biotechnology. *ACS Photon.* **9** (4), 1117–1126 (2022).
10. Koch, M., Mittleman, D. M., Ornk, J. & Castro-Camus, E. Terahertz time-domain spectroscopy. *Nat. Rev. Methods Primers* **3** (1), 48 (2023).
11. Hernandez-Cardoso, G. G., Singh, A. K. & Castro-Camus, E. Empirical comparison between effective medium theory models for the dielectric response of biological tissue at terahertz frequencies. *Appl. Opt.* **59** (13), D6 (2020).
12. Choy, T. C. *Effective Medium Theory: Principles and Applications* (Oxford University Press, 2015).
13. Wang, J., Lindley-Hatcher, H. & Chen, X. Pickwell-MacPherson, E. THz sensing of human skin: a review of skin modeling approaches. *Sensors* **21** (11), 3624 (2021).
14. Garet, F., Hofman, M., Meilhan, J., Simoens, F. & Coutaz, J. L. Evidence of Mie scattering at terahertz frequencies in powder materials. *Appl. Phys. Lett.* **105** (3) (2014).
15. Murphy, K. N., Markl, D., Nordon, A. & Naftaly, M. Observation of spurious spectral features in mixed-powder compressed pellets measured by terahertz time-domain spectroscopy. *IEEE Trans. THz Sci. Tech.* **13** (5), 569–572 (2023).
16. Kemp, M. C. Explosives detection by terahertz spectroscopy—a bridge too far? *IEEE Trans. THz Sci. Tech.* **1** (1), 282–292 (2011).
17. Hu, Y., Huang, P., Guo, L., Wang, X. & Zhang, C. Terahertz spectroscopic investigations of explosives. *Phys. Lett. A* **359** (6), 728–732 (2006).
18. Zaytsev, K. I. et al. The progress and perspectives of terahertz technology for diagnosis of neoplasms: a review. *J. Opt.* **22** (1), 013001 (2020).
19. Kucheryavenko, A. S. et al. Terahertz dielectric spectroscopy and solid immersion microscopy of ex vivo glioma model 101.8: brain tissue heterogeneity. *Biomed. Opt. Express* **12** (8), 5272–5289 (2021).
20. Martins, I. S. et al. Measurement of tissue optical properties in a wide spectral range: a review. *Biomed. Opt. Express* **14** (1), 249–298 (2023).
21. Tuchin, V. V., Zhu, D. & Genina, E. A. *Handbook of Tissue Optical Clearing: New Prospects in Optical Imaging* (CRC, 2022).
22. Kucheryavenko, A. S. et al. Terahertz-wave scattering in tissues: examining the limits of the applicability of effective-medium theory. *Phys. Rev. Appl.* **20** (5), 054050 (2023).
23. Joseph, C. S., Patel, R., Neel, V. A., Giles, R. H. & Yaroslavsky, A. N. Imaging of ex vivo nonmelanoma skin cancers in the optical and terahertz spectral regions. *J. Biophoton.* **7** (5), 295–303 (2014).
24. Xu, K. & Arbab, M. H. Terahertz polarimetric imaging of biological tissue: Monte Carlo modeling of signal contrast mechanisms due to Mie scattering. *Biomed. Opt. Express* **15** (4), 2328–2342 (2024).
25. Mitrofanov, O. et al. Near-field probing of Mie resonances in single TiO_2 microspheres at terahertz frequencies. *Opt. Express* **22** (19), 23034 (2014).
26. Choi, D. H., Kim, M., Park, D. W., Lee, E. S. & Lee, I. M. Broadband sub-wavelength terahertz subsurface imaging using a solid-immersion lens. *Opt. Laser Technol.* **174**, 110557 (2024).
27. Choi, D. H. Spatial and spectral beam characteristics in a terahertz broadband sub-wavelength imaging system using a solid immersion lens. *Appl. Opt.* **63** (13), 3619–3624 (2024).
28. García-Etxarri, A. et al. Strong magnetic response of submicron silicon particles in the infrared. *Opt. Express* **19** (6), 4815–4826 (2011).
29. Zhang, Y., Nieto-Vesperinas, M. & Sáenz, J. J. Dielectric spheres with maximum forward scattering and zero backscattering: a search for their material composition. *J. Opt.* **17** (10), 105612 (2015).
30. Hentschel, M. et al. Dielectric Mie voids: confining light in air. *Light Sci. Appl.* **12** (1), 3 (2023).
31. Naftaly, M. & Miles, R. E. Terahertz time-domain spectroscopy of silicate glasses and the relationship to material properties. *J. Appl. Phys.* **102** (4), 1 (2007).
32. Li, G. et al. Design and optimization of THz coupling in zirconia MAS rotors for dynamic nuclear polarization NMR. *J. Magn. Reson.* **364**, 107722 (2024).
33. Jepsen, P. U. & Keiding, S. R. Radiation patterns from lens-coupled terahertz antennas. *Opt. Lett.* **20**, 807–809 (1995).
34. Podzorov, A., Wojdyla, A. & Gallot, G. Beam waist measurement for terahertz time-domain spectroscopy experiments. *Opt. Lett.* **35**, 901–903 (2010).
35. Coutaz, J., Garet, F. & Wallace, V. *Principles of Terahertz Time-Domain Spectroscopy* (Pan Stanford, 2018).
36. Son, H., Choi, D. H. & Park, G. S. Improved thickness estimation of liquid water using kramers–Kronig relations for determination of precise optical parameters in terahertz transmission spectroscopy. *Opt. Express* **25** (4), 4509–4518 (2017).

Acknowledgements

The study was funded by Electronics and Telecommunications Research Institute (24YB2310, 24ZB1320).

Author contributions

D.-H.C. conceived the project, conducted experiments and simulations, analyzed the data and wrote the manuscript.

Declarations

Competing interests

The authors declare no competing interests.

Additional information

Correspondence and requests for materials should be addressed to D.-H.C.

Reprints and permissions information is available at www.nature.com/reprints.

Publisher's note Springer Nature remains neutral with regard to jurisdictional claims in published maps and institutional affiliations.